Mutual Information-Based CT-MR Brain Image Registration Using Generalized Partial Volume Joint Histogram Estimation

Hua-mei Chen and Pramod K. Varshney*, *Fellow, IEEE*

***Abstract*—Mutual information (MI)-based image registration has been found to be quite effective in many medical imaging applications. To determine the MI between two images, the joint histogram of the two images is required. In the literature, linear interpolation and partial volume interpolation (PVI) are often used while estimating the joint histogram for registration purposes. It has been shown that joint histogram estimation through these two interpolation methods may introduce artifacts in the MI registration function that hamper the optimization process and influence the registration accuracy. In this paper, we present a new joint histogram estimation scheme called generalized partial volume estimation (GPVE). It turns out that the PVI method is a special case of the GPVE procedure. We have implemented our algorithm on the clinically obtained brain computed tomography and magnetic resonance image data furnished by Vanderbilt University. Our experimental results show that, by properly choosing the kernel functions, the GPVE algorithm significantly reduces the interpolation-induced artifacts and, in cases that the artifacts clearly affect registration accuracy, the registration accuracy is improved.**

***Index Terms*—Image registration, interpolation-induced artifacts, joint histogram estimation, mutual information, registration of brain CT and MR images.**

I. Introduction

MULTIMODALITY image registration has become an important research topic because of its great value in a variety of applications. For medical image analysis, an image showing functional and metabolic activity—such as single photon emission computed tomography (SPECT), positron emission tomography (PET), and magnetic resonance spectroscopy (MRS)—is often registered to an image which shows anatomical structures, such as magnetic resonance image (MRI), computed tomography (CT), and ultrasound. These registered multimodality images lead to improved diagnosis, better surgical planning, more accurate radiation therapy and countless other medical benefits [1]. Existing image registration techniques can be broadly classified into two categories: feature-based and intensity-based methods [2]. A feature-based method requires the extraction of features common in both images. Obviously, a feature-based method is data dependent. Since different image data may have different features, the feature extraction algorithms adopted in a feature-based image registration algorithm are expected to be different for different registration tasks. In contrast, intensity-based image registration techniques are free from this limitation because they do not deal with the identification of geometrical landmarks. The general design criterion of an intensity-based image registration technique can be expressed as

$$\alpha^* = \arg opt\,(S\,(F(\mathbf{x}), R\,(T_\alpha(\mathbf{x}))))\tag{1}$$

where R and F are the images to be registered. $T\alpha$ is the transformation, characterized by the pose parameters α, that will be applied to the coordinates of each grid point $\mathbf{x}$ in F. S is an intensity-based similarity measure calculated over the region of overlap of the two images. The above criterion says that the two images F and R are registered through ${T_\alpha}^*$ when α^* optimizes the selected similarity measure S. Among a variety of existing similarity measures, mutual information (MI) has received substantial attention recently because of its ability to measure the similarity between images from different modalities, especially in, but not limited to, medical imaging applications [3]–[8].

Many aspects of the use of MI as the similarity measure to be maximized have been studied. In [9]–[11], three variations of MI are proposed to provide an overlap-invariant measure. In [12], maximization of MI is found to be a maximum likelihood estimation problem under very minimal assumptions. In [13], a multiresolution optimization approach using an optimizer specifically designed for the MI measure is presented. In [14], a multivariate MI measure is proposed to increase the accuracy provided that at least two highly accurate pre-registered images are available. In [15], an upper bound is derived to provide useful insights about the use of MI as a similarity measure. Finally, a phenomenon called interpolation artifacts that may appear in MI-based registration functions is studied in [16].

In [16], it is pointed out that, under certain circumstances, discussed in Section III, existing joint histogram estimation methods may result in different types of artifact patterns in a MI-based registration function. In that study, two joint histogram estimation methods were examined: linear interpolation and partial volume interpolation (PVI) [4]. It was shown that both methods may result in significant artifact patterns that introduce spurious local

Manuscript received October 25, 2001; revised March 3, 2002. This work was supported in part by the Air Force Research Laboratory, Air Force Materiel Command, USAF, under Grant F30602-95-1-0027 and in part by the Defense Advanced Research Project Agency (DARPA) under Grant N66001-99-1-8922. The Associate Editor responsible for coordinating the review of this paper and recommending its publication was C. Meyer. *Asterisk indicates corresponding author.*

H.-M. Chen is with the Department of Computer Science and Engineering, University of Texas at Arlington, Arlington, TX 76019 USA (e-mail: hchen@cse.uta.edu).

*P. K. Varshney is with the Department of Electrical Engineering and Computer Sciences, Syracuse University, Syracuse, NY 13244 USA (e-mail: varshney@syr.edu).

Digital Object Identifier 10.1109/TMI.2003.816949

0278-0062/03$17.00 © 2003 IEEE

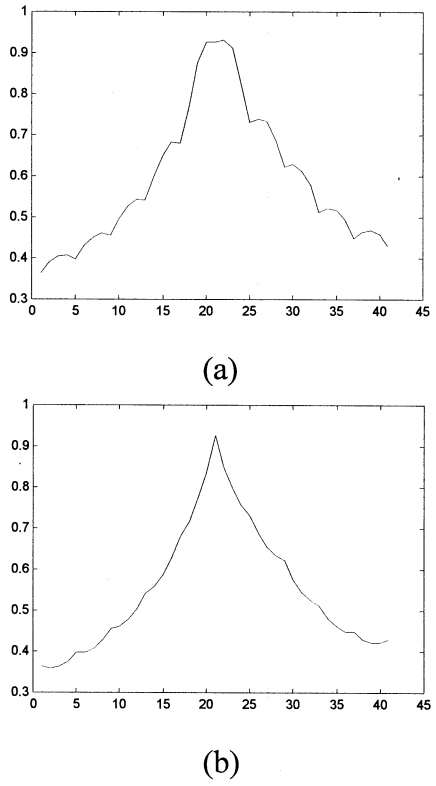

Fig. 1. Typical interpolation-induced artifact patterns for a MI-based registration function. In both cases, the vertical axis is the MI-based measure and the horizontal axis can be x or y or z displacement. (a) Artifact pattern resulting from linear interpolation. (b) Artifact patter resulting from PVI algorithm.

maxima. Typical artifact patterns resulting from these two joint histogram estimation methods are shown in Fig. 1. These artifact patterns have also been found when clinically obtained brain images are used. In addition to the linear interpolation and PVI, we have found similar patterns when other image intensity interpolation methods like cubic convolution interpolation [17] and cubic B-spline interpolation [18], [19] are used [20]. Artifact patterns have at least two consequences: 1) they hamper the global optimization process because of the introduction of many local extrema and 2) they influence registration accuracy [16] because the true global optimum is now buried under the artifact pattern. However, this influence is not always negative, i.e., registration accuracy does not always become worse. It depends on the position of the highest peak of the artifact pattern. To facilitate explanation, let α_{ideal} denote the pose parameters (which is a vector in a multidimensional search space) that result in perfect registration, $\alpha_{\text{arti}-\text{free}}$ the pose parameters found using an artifact-free MI-based registration algorithm and α_{arti} the pose parameters resulting from a MI-based registration algorithm that is known to suffer from the artifacts due to the use of an algorithm such as the PVI algorithm. Clearly, α_{arti} is determined by the position of the highest peak of the artifact pattern. If this position α_{arti} happens to be closer than $\alpha_{\text{arti}-\text{free}}$ to α_{ideal}, the influence of the artifacts on the registration accuracy is positive, i.e., the registration accuracy is improved. On the other hand, if the distance between α_{arti} and α_{ideal} is larger than that between $\alpha_{\text{arti}-\text{free}}$ and α_{ideal}, the influence is negative and the registration accuracy becomes worse. Therefore, *assuming perfect optimization, registration accuracy would depend on the position of the highest peak of the artifact pattern*. Although the influence is not always negative, it is still desirable to develop an artifact-free MI-based registration algorithm. There are two reasons: 1) an artifact-free MI-based registration algorithm facilitates the global optimization process; and 2) when the influence of the artifacts on the registration accuracy is negative, artifact-free MI-based registration can improve registration accuracy. In general, it is difficult to gauge whether the influence is positive or negative. This influence on registration accuracy is at most half the size of a voxel [16]. To assess the influence of the artifacts on registration accuracy, a peak-shift (*PS*) measure is devised in this paper (Section VI). From our experiments, it seems reasonable to consider the influence to be negative if the *PS* measure is equal to or larger than 0.5. The goal of this paper is to develop an artifact-free, or nearly artifact-free MI-based registration algorithm to improve registration accuracy when the influence of the artifacts on registration accuracy is negative.

Provided in Section II, the MI measure between two images is solely determined by their joint histogram. In this paper, we have developed a new joint histogram estimation scheme named generalized partial volume estimation (GPVE). This method generalizes the PVI algorithm proposed by Collignon and Maes [4] by incorporating it into a larger framework. In this framework, a kernel function is employed in each of the x, y, and z directions to estimate the joint histogram of two image volumes. It can be shown that the PVI algorithm is a special case corresponding to the use of the first-order B-spline as the kernel function in each direction. We have applied it to the clinically obtained brain CT and MR image data furnished by Vanderbilt University [21], [22]. The evaluation of the proposed GPVE algorithm is based on its comparison with the PVI algorithm. Our experimental results show that, by choosing the second-order or the third-order B-spline as the kernel function along the direction(s) in which the artifacts would occur if the PVI algorithm were applied, the artifacts can be reduced significantly for CT to MR brain image registration. In cases where the *PS* measure is equal to or larger than 0.5 when PVI is employed, registration accuracy can be improved significantly using a higher order kernel along the direction(s) in which artifacts occur.

This paper is organized as follows. In Section II, we review the theoretical background of MI-based image registration methods. In Section III, a brief description of interpolation-induced MI artifacts is presented. The proposed joint histogram estimation scheme, GPVE, is presented in Section IV. A comparison of the computational complexities of different interpolation schemes is provided in Section V. Registration accuracies of higher order GPVE algorithms are compared with that of the PVI algorithm in Section VI using the Vanderbilt CT and MR brain image data. Finally, some concluding remarks are given in Section VII.

II. Mutual Information Based Image Registration

MI has its roots in information theory [23]. The MI of two random variables A and B is defined by

$$I(A,B) = \sum_{a,b} P_{A,B}(a,b) \log \frac{P_{A,B}(a,b)}{P_A(a) \cdot P_B(b)} \qquad (2)$$

where $P_A(a)$ and $P_B(b)$ are the marginal probability mass functions and $P_{A,B}(a,b)$ is the joint probability mass function. MI measures the degree of dependence of A and B by measuring the distance between the joint distribution $P_{A,B}(a,b)$ and the distribution associated with the case of complete independence $P_A(a) \cdot P_B(b)$, by means of the relative entropy or the Kullback-Leibler measure [23]. MI is related to entropies by

$$I(A,B) = H(A) + H(B) - H(A,B) \quad (3)$$
$$= H(A) - H(A \mid B) \quad (4)$$
$$= H(B) - H(B \mid A) \quad (5)$$

with $H(A,B)$ being their joint entropy; $H(A)$ and $H(B)$, the entropies of A and B; and $H(A \mid B)$ and $H(B \mid A)$, the conditional entropies of A given B and of B given A, respectively. The definitions of these entropies are

$$H(A) = -\sum_a P_A(a) \cdot \log P_A(a) \quad (6)$$
$$H(A,B) = -\sum_{a,b} P_{A,B}(a,b) \cdot \log P_{A,B}(a,b) \quad (7)$$
$$H(A \mid B) = -\sum_{a,b} P_{A,B}(a,b) \cdot \log P_{A|B}(a \mid b) \quad (8)$$

To employ MI as a similarity measure, we need to utilize the concept of the two-dimensional (2-D) histogram of an image pair, the joint histogram. The joint histogram h of an image pair can be defined as a function of two variables, A, the gray-level intensity in the first image and B, the gray-level intensity in the second image. Its value at the coordinate (A,B) is the number of corresponding pairs having gray-level A in the first image and gray-level B in the second image. The joint probability mass function used in the calculation of MI of an image pair can then be obtained by normalizing the joint histogram of the image pair as

$$P_{A,B}(a,b) = \frac{h(a,b)}{\sum_{a,b} h(a,b)} \quad (9)$$

From the joint probability mass function, we may obtain the two marginal probability mass functions directly as

$$P_A(a) = \sum_b P_{A,B}(a,b) \quad (10)$$
$$P_B(b) = \sum_a P_{A,B}(a,b). \quad (11)$$

The MI registration criterion states that the image pair is geometrically aligned through a geometric transformation T when $I(A(\mathbf{x}), B(T(\mathbf{x})))$ is maximal. Notice that the marginal entropies in (3) change with transformation T because the image overlap changes. The strength of the MI similarity measure lies in the fact that no assumptions are made regarding the nature of the relation between the image intensities in both modalities, except that such a relationship exists.

From (2) and (9)–(11), we can see that the joint histogram of an image pair is the only quantity required to calculate the MI between them. As a result, the quality of the estimated joint histogram solely determines the accuracy of this method.

Intuitively, the joint histogram can be estimated by a two-step procedure. Denote the two images that need to be registered as F, the floating image on which a geometric transformation will be applied and R, the reference image that will be interpolated. The first step is to estimate the intensity values in R at every transformed grid point of F by employing an intensity interpolation algorithm. The second step is then to determine the joint histogram from the overlap of the floating image and the interpolated reference image. In practice, each interpolated intensity value needs to be rounded to the nearest integer so that the joint histogram can be obtained by a simple counting procedure. It is shown in [4] that the MI registration function obtained by using linear interpolation usually is not very smooth. To overcome this nonsmoothness, Collignon and Maes proposed a joint histogram estimation scheme called PVI [4]. By using this method, a smooth MI registration function can be obtained.

A recent study [16] pointed out that both of the methods mentioned above may result in certain types of artifacts in the MI registration function as shown in Fig. 1. This has been confirmed clinically [16]. In Section III, the conditions under which the artifacts occur are discussed.

III. Interpolation-induced Artifacts

It has been pointed out in [16] that when two images have equal sample spacing in one or more dimensions, existing joint histogram estimation algorithms like PVI and linear interpolation may result in certain types of artifact patterns in a MI-based registration function. More precisely, the artifacts will occur when the ratio of the two sample spacings along a certain dimension is a simple rational number. The reason is that in this case, many of the grid planes (or grid lines for 2-D images) may be aligned along that dimension under certain geometric transformations. Therefore, fewer interpolations are needed to estimate the joint histogram of these two images than in the case that none of the grid planes are aligned. For example, when the ratio of voxel sizes of the two image volumes along the z axis are 5 (mm)/3 (mm) and 1 (mm)/1 (mm) along the other two axes, then by shifting one of the image volumes, the grids on planes 1,4,7,… of the first image volume (the one with volume size 5 mm along the z axis) can be made to coincide with the grids on planes 1, 6, 11,…, of the second image volume. In this case, the contribution of the coincident grids to the joint histogram can be counted directly without resorting to any form of estimation. But if one of the image volumes is further shifted a little bit along the z axis, then none of the grids of the two image volumes will be coincident with each other and the joint histogram has to be estimated completely. In this case, this sudden change between "fewer " estimation and "substantially more" estimation causes the artifacts. Also, the artifacts are expected to repeat for every 1 mm in the z direction because in this case, there are certain grid planes that will be aligned for every 1-mm shift in the z direction. One example is presented in Fig. 2. Simulated brain MR T1 image with voxel size $1\ \mathrm{mm} \times 1\ \mathrm{mm} \times 5\ \mathrm{mm}$ and MR T2 image with voxel size $1\ \mathrm{mm} \times 1\ \mathrm{mm} \times 3\ \mathrm{mm}$ from BrainWeb

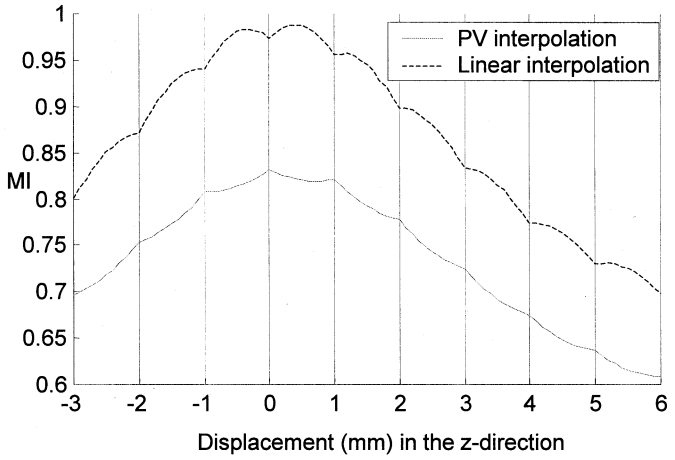

Fig. 2. Artifact patterns in the case where the ratio of sample spacings equal 5/3.

[24], [25] are used to produce the artifact patterns. Notice that the artifacts occur for every 1-mm spacing as expected.

It is pointed out that abrupt changes in the joint histogram dispersion resulting from the PVI method for grid-aligning transformations cause the concave artifact pattern [16]. Based on this, we believe a joint histogram estimation scheme that reduces the degree of sudden changes in joint histogram dispersion is able to reduce the artifacts. In Section IV, we describe such an algorithm by generalizing the PVI algorithm.

IV. Generalized Partial Volume Estimation

Before presenting the GPVE algorithm, let us first review the PVI algorithm proposed by Maes and Collignon [4] in the 2-D case. This will set the stage for our algorithm by providing some of the terminology used.

Let F and R be the floating image and reference image, respectively, that can be considered as two mappings

$$F : \mathbf{x} \rightarrow F(\mathbf{x}), \mathbf{x} \in X$$
$$R : \mathbf{y} \rightarrow R(\mathbf{y}), \mathbf{y} \in Y \tag{12}$$

where X is the discrete domain of F and Y is the discrete domain of R. The value $F(\mathbf{x})$ represents the intensity of the floating image at the grid point with coordinate $\mathbf{x} = (x_i, x_j)$ in terms of the sample spacing. Now if we let $T\alpha$ be the transformation characterized by the parameter set α that is applied to the grid points of F and assume that $T\alpha$ maps the grid point (x_i, x_j) in image F onto the point with coordinate, in terms of sample spacing, $(y_i + \Delta_i, y_j + \Delta_j)$ in the image R, where (y_i, y_j) is a grid point in R and $0 \leq \Delta_i, \Delta_j < 1$. In Fig. 3, $\mathbf{y}_1, \mathbf{y}_2, \mathbf{y}_3, \mathbf{y}_4$ are the grid points on the reference image R that are closest to the transformed grid point $T_\alpha(\mathbf{x})$. $T_\alpha(\mathbf{x})$ splits the cell $\mathbf{y}_1, \mathbf{y}_2, \mathbf{y}_3, \mathbf{y}_4$ into four subcells. The subcells have areas $\omega_1, \omega_2, \omega_3$ and ω_4 as shown with the constraint $\sum_{l=1}^{4} \omega_l(T_\alpha(\mathbf{x})) = 1$. The PVI algorithm obtains the joint histogram as follows:

$$h\left(F(\mathbf{x}), R\left(\mathbf{y}_l\right)\right) += \omega_l \text{ for } l = 1 \ldots 4 \tag{13}$$

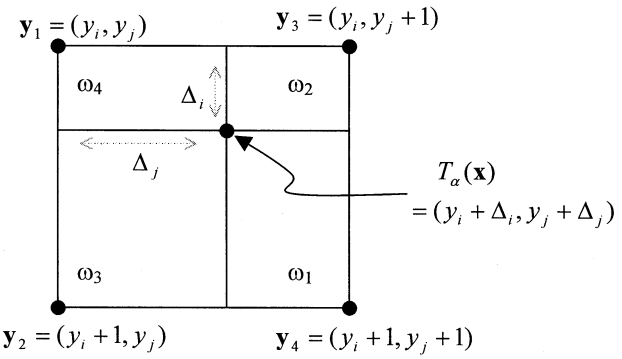

Fig. 3. Graphical illustration of the PVI algorithm in 2-D space.

Let f be a triangular function defined by

$$f(t) = \begin{cases} 1 - t, & \text{if } 0 \leq t \leq 1 \\ 1 + t, & \text{if } -1 \leq t < 0 \\ 0, & \text{otherwise} \end{cases} . \tag{14}$$

then we can rewrite (13) as

$$h(F(x_i, x_j), R(y_i + p, y_j + q)) + = f(p - \Delta_i) \cdot f(q - \Delta_j) \quad \forall p, q \in Z \tag{15}$$

p and q are used to specify the pixels involved in the histogram updating procedure. Notice that in (15), the increments are all zeros except when $p, q \in \{0, 1\}$. In fact, when $p = 0$ and $q = 0$, the pixel under consideration is $\mathbf{y}_1$ and the corresponding increment is ω_1. When $p = 1$ and $q = 0$, the pixel under consideration is $\mathbf{y}_2$ and the corresponding increment is ω_2. When $p = 0$ and $q = 1$, the pixel under consideration is $\mathbf{y}_3$ and the corresponding increment is ω_3. Finally, when $p = 1$ and $q = 1$, the pixel under consideration is $\mathbf{y}_4$ and the corresponding increment is ω_4. Now the proposed GPVE algorithm for the three-dimensional (3-D) case is ready to be presented in terms of a more general kernel function.

Let f be a real valued function satisfying

$$1)\ f(x) \geq 0, \text{ where } x \text{ is a real number} \tag{16}$$

$$2)\ \sum_{n=-\infty}^{\infty} f(n - \Delta) = 1, \text{ where } n \text{ is an integer, } 0 \leq \Delta < 1 \tag{17}$$

then for each grid point $\mathbf{x} = (x_i, x_j, x_k) \in X$ in the image volume F, the joint histogram h is updated in the following manner:

$$h(F(x_i, x_j, x_k), R(y_i + p, y_j + q, y_k + r)) + = f(p - \Delta_i) \cdot f(q - \Delta_j) \cdot f(r - \Delta_k) \quad \forall p, q, r \in Z \tag{18}$$

where f is referred to as the kernel function of GPVE and Z is the set of all integers.

Notice that the increment (contribution of each voxel involved) of the joint histogram is now represented in terms of the kernel functions along each direction. The first condition on f ensures that the increments are nonnegative while the second condition makes the sum of the updated amounts equal to one for each corresponding pair of points (x_i, x_j, x_k) in F and $(y_i + \Delta_i, y_j + \Delta_j, y_k + \Delta_k)$ in R.

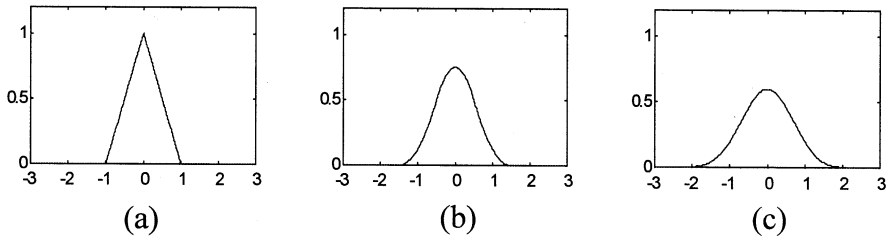

Fig. 4. B-splines. (a) First order. (b) Second order. (c) Third order.

From this generalization, we can see that the PVI algorithm proposed by Maes *et al.* is a special case when f is a triangular function defined by (14). Here, we propose to use B-splines as the kernel function f because it satisfies both the conditions in (16) and (17) and furthermore, it has finite support. Fig. 4 shows the shapes of the first-, second-, and third-order B-splines. From the shapes of the B-splines, it should be noticed that the kernel function introduced in (16) and (17) is an approximator rather than an interpolator because an interpolator has zero crossings at positions 0, ± 1, ± 2, ... The kernel function is introduced to assign a value to the contribution of each voxel involved in updating the joint histogram. For more details on B-spline functions, interested readers are referred to [18], [19]. It is interesting to point out that the triangular function defined in (14) is identical to the first-order B-spline function. Therefore, the PVI algorithm is actually equivalent to the first-order GPVE algorithm.

Fig. 5 shows the grids in R (shown as "$\circ$") that are involved in updating the joint histogram in 2-D case using the first-, second-, and third-order B-splines as the kernel function. In each case, the transformed grid point $T_\alpha(\mathbf{x})$ appears at the center of each plot. Fig. 5(a) shows the case when the transformed grid point of F is coincident with a grid point of R and Fig. 5(b) shows the case when the transformed grid point of F is not a grid point in R but surrounded by four grid points in R.

In the GPVE algorithm, the kernel functions can be different along different directions. That is, we can rewrite (18) as

$$h(F(x_i, x_j, x_k), R(y_i + p, y_j + q, y_k + r)) + = f_1(p - \Delta_i) \cdot f_2(q - \Delta_j) \cdot f_3(r - \Delta_k) \quad \forall p, q, r \in Z \quad (19)$$

where f_1, f_2 and f_3 can be different kernels. For example, if we know that the artifact is going to appear in the z direction only, then we can choose both f_1 and f_2 as the first-order B-spline but choose f_3 as the third-order B-spline. This is justified by the experiments in Section VI.

From Fig. 5 we observe that, in the 2-D case, one to four entries of the joint histogram are involved in updating for each pixel in F if PVI (or the first-order GPVE) is used. This is evident from the leftmost figures of Fig. 5(a) and (b). In Fig. 5(a), only the center pixel is involved in updating whereas in Fig. 5(b) all the four grid points surrounding the point marked by "*" are involved in updating. Similarly, nine and four grid points are involved in updating in Fig. 5(a) and (b), respectively, when second-order GPVE is employed. The number of grid points involved in updating is determined by the size of the support of the kernel function, which is shown as the shaded area in Fig. 5(a) and 5(b). The length of each side of the shaded region for the case of third-order GPVE is 4 times of the sample spacing. In this case, 9–16 grid points are involved in updating as seen in Fig. 5. The ratios of the maximum number to minimum number of updated entries are 4, 2.25 and 1.78 when using the first-, second–, and third-order GPVE, respectively. In the 3-D case, the corresponding ratios are 8, 3.375, and 2.370. The reduction in the values of these ratios when higher order kernels are employed gives it the ability to reduce the artifacts, since now a certain degree of joint histogram dispersion is introduced by the higher order kernel even when the grid points of the two images are perfectly aligned. This reduces the sudden changes of the joint histogram dispersion. Intuitively, the ratio needs to be one to remove the artifacts completely because different numbers of updated entries introduce different amounts of dispersion of the joint histogram. However, based on our experiments presented in Section VI, the artifacts can be hardly seen when either the second- or third-order GPVE is used.

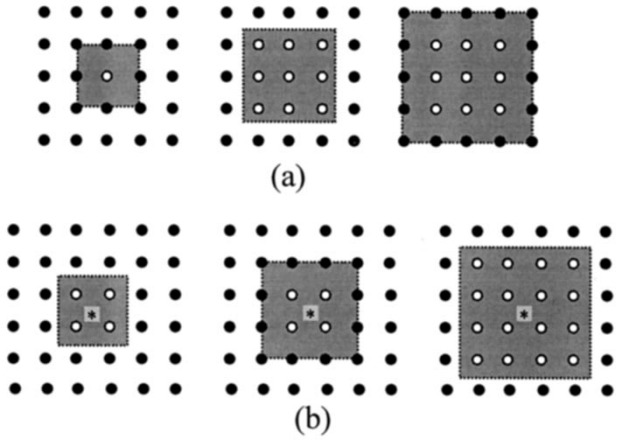

Fig. 5. Grid points corresponding to R that are involved in updating the joint histogram in the 2-D case. (a) When the transformed grid point is coincident with a grid point in R. (b) When the transformed grid point is surrounded by grid points in R.

V. Computational Complexity

When calculating the MI of two images, much of the computational power is consumed while estimating the joint histogram; therefore, our analysis of the computational complexity will focus on the estimation of the joint histogram only. A comparison of the execution times for PVI and GPVE algorithms is also reported in this section.

TABLE I
EXECUTION TIMES FOR PVI, SECOND-ORDER GPVE, AND THIRD-ORDER GPVE ALGORITHMS

Algorithm	PVI	2nd GPVE along z only	3rd GPVE along z only	2nd GPVE along x, y, z	3rd GPVE along x, y, z
Execution time (sec)	4.63	5.43	5.65	12.15	13.42
Ratio	1	1.17	1.22	2.62	2.90

A B-spline of order n can be generated by convolving the B-spline of order 0 with itself $(n+1)$ times [18]. That is:

$$\beta^n(x) = \beta^{n-1} * \beta^0(x) = \underbrace{\beta^0 * \beta^0 * \cdots * \beta^0(x)}_{n+1\ times} \tag{20}$$

where $\beta^n(x)$ is the nth order B-spline and $\beta^0(x)$ is nothing but a rectangular pulse of the following form:

$$\beta^0(x) = \begin{cases} 1 & \text{if } -0.5 \le x < 0.5 \\ 0 & \text{otherwise} \end{cases} \tag{21}$$

Therefore, the computational complexity of each evaluation of the nth order B-spline function is basically O(n). Observing Figs. 4 and 5 we know that the size of the support of the nth order B-spline function along each dimension is $n+1$. This means that the evaluation of the nth order B-spline function is performed $(n+1)^3$ times (in the 3-D case) to update the joint histogram for each pixel in the floating image within the overlap region. Thus, the entire computational load is $O(n) \times O((n+1)^3)$ if the nth order B-spline function is used along all the three x, y, and z directions. The ratios of the computational complexities for $n = 1$, 2, 3 in this case are 1:6.75:24. For our application, fortunately, as shown in the next section, the higher order kernel is required in the z direction only. This reduces the computational load to $O(n) \times O(n+1)$. Hence, the ratios of the computational complexities for $n = 1$, 2 and 3 become 1:3:6. To further reduce the computational load, we use a simple table lookup strategy to avoid the evaluation of the B-spline functions. We stored the values of the nth order B-spline in a lookup table from $-(n+1)/2$ to $(n+1)/2$ with increments equal to 0.001. In this manner, the evaluation of the nth order B-spline becomes a simple table lookup task and the computational load is further reduced to $O(n+1)$. The final ratios of the computational complexities for $n = 1$, 2, and 3 are, therefore, 1:1.5:2.

In our implementation, we use a code written using both MATLAB and Microsoft Visual C++. To compare the execution times of the PVI, the second-order GPVE, and the third-order GPVE algorithm, we use the simulated brain images from BrainWeb [24], [25]. The overlap region is kept as $[170 \times 206 \times 130]$ in all cases. Our platform is Dell Precision 530 with 1.8-GHz Intel Xeon CPU. The execution times for the computation of the MI measure using PVI, second-order GPVE along the z direction only, third-order GPVE along the z direction only, second-order GPVE along x, y, and z directions, and third-order GPVE along x, y, and z directions are reported in Table I.

VI. EXPERIMENTAL RESULTS

We have implemented the first-, second-, and third-order GPVE algorithms as a part of the MI-based image registration algorithm for brain CT to MR image registration application using clinical image data furnished by Vanderbilt University. The results of our experimental study are presented in this section. Registration results obtained by using a fiducial-based registration [26] serve as the gold standard that was not available to us. Registration results that we obtained were sent to Vanderbilt University where they compared our results with the gold standard and provided us the accuracy measurements achieved by our algorithm. Registration error reported in all tables in this section is the TRE value provided by Vanderbilt. For an in depth description of this database and the procedure used to evaluate a participant's registration results, please see [21], [22]. The estimated error of the gold standard is $\sim$ 0.39 mm for CT to MR registration [21]. In our implementation, both CT and MR image intensities have been linearly binned into 256 gray-levels and normalized MI is employed as the similarity measure because it has been shown that it is more likely to be overlap invariant for medical brain imaging applications [9]. Multiresolution optimization approach using the simplex search algorithm [27] is employed to determine the maximum of the MI similarity measure. The procedure terminates when the standard deviation of each transformation parameter of the final simplex is less than 0.001 degree for rotations or 0.001 mm for displacements. There are two parts in our experiments. In the first part, a practice data set (PD) provided by Vanderbilt University, for which the gold standard was available to us, is used to perform a preliminary test. There is only one subject in the PD for each registration task. The voxel sizes for this PD are listed in Table II. From Table II, we know that the z direction is the only possible direction along which the artifacts could occur, because of the identical slice thickness of the CT image volume and the nonrectified MR image volumes. Experiments with four different implementations of the algorithm are performed on this data set. Each implementation involves a unique choice of the kernel functions. The four implementations are second-order GPVE along the z direction and first-order GPVE along x and y directions, second-order GPVE along all x, y, and z directions, third-order GPVE along the z direction and first-order GPVE along x and y directions and third-order GPVE along all x,

TABLE II
VOXEL SIZES OF THE PD

	voxel size in mm
CT	[0.653595×0.653595×4]
PD, T1, T2	[1.25×1.25×4]
PD_rf	[1.263903×1.263903×4.1024]
T1_rf	[1.266464×1.266464×4.0556]
T2_rf	[1.271×1.271×4.0728]

TABLE III
REGISTRATION ERRORS FOR PART 1 OF THE EXPERIMENTS

Practice Data Set	2nd GPVE along z only	2nd GPVE along x, y , z	3rd GPVE along z only	3rd GPVE along x, y, z
	error (mm)	error (mm)	error (mm)	error (mm)
CT_PD	2.6493	2.7330	2.7009	2.7710
CT_T1	1.3189	1.3022	1.1149	1.1270
CT_T2	3.7963	3.8438	3.7749	3.8099
CT_PDrf	3.5656	3.5576	3.3925	3.3875
CT_T1rf	1.5403	1.5320	1.4484	1.3819
CT_T2rf	2.5215	2.4975	2.5099	2.5103

TABLE IV
REGISTRATION ERRORS FOR CT-PD IMAGE DATA

CT-PD	first order		second order	third order
	error (mm)	visual influence on accuracy (*PS*)	error (mm)	error (mm)
patient_001	1.9977	mild (0.2)	1.9228	1.9153
patient_002	1.2299	no	1.2432	1.2937
patient_003	2.0026	mild (0.1)	1.8938	1.7069
patient_004	3.6220	no	2.9257	2.8353
patient_005	1.8771	*mild* (0.2)	1.9415	2.0097
patient_006	1.5194	strong (0.6)	0.5897	0.5851
patient_007	1.4789	*mild* (0)	1.4535	1.4933

TABLE V
REGISTRATION ERRORS FOR CT-T1 IMAGE DATA

CT-T1	first order		second order	third order
	error (mm)	visual influence on accuracy	error (mm)	error (mm)
patient_001	1.7707	mild (0.3)	1.2560	1.2345
patient_002	1.2745	strong (0.7)	0.8215	0.8475
patient_003	1.2328	*mild* (0)	1.3173	1.3035
patient_004	2.9410	strong (1.2)	1.7740	1.8078
patient_005	1.3967	mild (0.4)	1.2782	1.3057
patient_006	1.3469	mild (0.2)	1.033	0.9188
patient_007	0.8950	*mild* (0)	1.002	1.0683

TABLE VI
REGISTRATION ERRORS FOR CT-T2 IMAGE DATA

CT-T2	first order		second order	third order
	error (mm)	visual influence on accuracy (*PS*)	error (mm)	error (mm)
patient_001	2.1906	*mild* (0.1)	2.7672	2.8046
patient_002	1.5538	no	1.7799	1.8891
patient_003	1.3920	mild (0.2)	1.2336	1.2265
patient_004	2.7021	no	2.6294	2.7959
patient_005	1.7265	*mild* (0.2)	1.9959	1.9801
patient_006	1.2842	strong (0.5)	0.6738	0.6729
patient_007	1.2173	*mild* (0)	1.6573	1.7857

y, and z directions. Table III shows the results. The purpose of this experiment is to experimentally verify our statement in Section IV that we need to employ the higher order kernel only in the direction along which the artifacts are expected to occur. From Table III, we can observe that the registration results are essentially the same when higher order kernels are applied along either all of the three axes or along the z axis only. This observation verifies our statement made about the selection of the kernel function in each direction. Since the use of a higher order kernel is more computationally intensive, it suffices to use it in only the direction that is likely to produce artifacts. It is computationally more efficient without sacrificing registration accuracy.

In the second part of the experiments, we compare the registration errors obtained by PVI with those obtained by higher order GPVE. Tables IV–VI show the results of CT-PD, CT-T1 and CT-T2 image registrations for patient_001-patient_007 data using first-, second-, and third-order GPVE algorithms. Each higher order GPVE is performed along z coordinate only because it is the direction in which artifacts could possibly occur. We have shown that it is sufficient to do so in the first part of the experiments. Entries in the columns entitled "visual influence on accuracy" indicate whether or not the results obtained from using the first-order GPVE (PVI) suffer from the artifacts. It can be determined by observing the plot of the registration function along the z axis (the direction along which artifacts may occur) after registration. One example is given in Fig. 6, which shows the plots of the registration functions of CT-PD registration for patient_004, patient_005 and patient_006 data sets. Three indicators {no, mild, strong} are used to describe the influence of the artifacts on the registration accuracy by visually examining the registration functions obtained. The entry "no" indicates that no artifacts are observed as shown in Fig. 6(a). In Fig. 6(b), although the artifact pattern is observable, the position of the true global maximum is expected to be very close to the position of the maximum determined in the presence of the artifacts. In this case, "mild" is used to indicate that the artifact pattern is present but its influence on the accuracy is *uncertain*. In other words, the influence on the registration accuracy can possibly be positive, as explained in the introduction section. Finally, in Fig. 6(c) this influence is large and is most likely to decrease the registration accuracy. In this case, "strong" is entered in the "visual influence on accuracy" column. To help distinguish the "strong" from the "mild," we use cubic convolution interpolation to interpolate the MI value from -4 mm to 4 mm and define a *PS* measure for each case where the artifacts are observable as shown in Fig. 6(b) and (c). The *PS* measure is defined as the distance between the position of the highest peak determined in the presence of artifacts and the position of the maximum value determined by the interpolated curve. We classify it as a "strong" case if the *PS* measure is no less than 0.5 mm; otherwise, it is classified as a "mild" case. In Fig. 6(b) and (c), the *PS* measures are 0.2 and 0.6 mm, respectively. In Tables IV–VI, the numbers in the "visual influence on accuracy" column provide this *PS* measure for each case. We want to point out here that the *PS* measure defined above is used to help *visually* judge the influence of the artifacts on the registration accuracy. It is by no means an absolute measurement of the influence of the artifacts on the registration accuracy. From Tables IV–VI, we can observe that in cases when "strong" is entered in the "visual influence on accuracy" column, the use of the second- or third-order GPVE obviously improves registration accuracy. We believe it is because the influences of the artifacts on the registration accuracy are negative in those cases. The use of higher order GPVE significantly reduces the artifacts and therefore, the accuracies are improved. Figs. 7 and 8 show the registration functions using the same image data as in Fig. 6 but second- and third-order GPVE are used. From them we see that artifacts are no longer observed. The mean registration errors in this case are 1.7548, 0.9648, and 0.9783 mm for the first second and third GPVE,

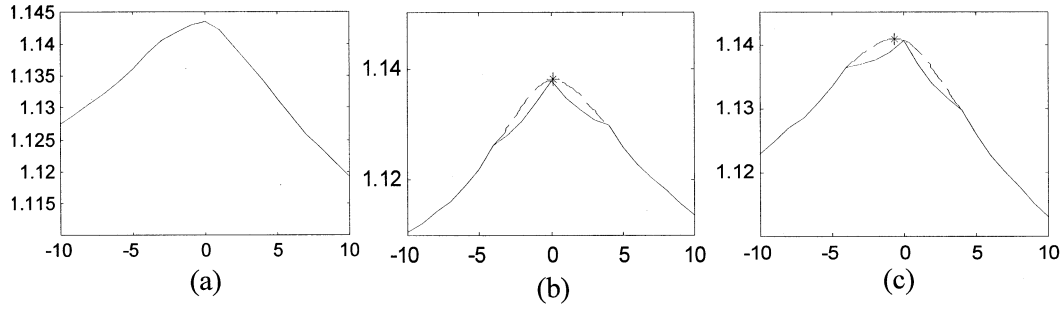

Fig. 6. Registration functions for CT_PD registration of patient_004 $\sim$ patient_006 data sets. The indicators in the "visual influence on accuracy" columns in Tables V–VIII are "no," "mild," and "strong," respectively, to specify the influence of the artifacts on the registration accuracy. In each case, x axis is the displacement in mm and y axis is the MI measure.

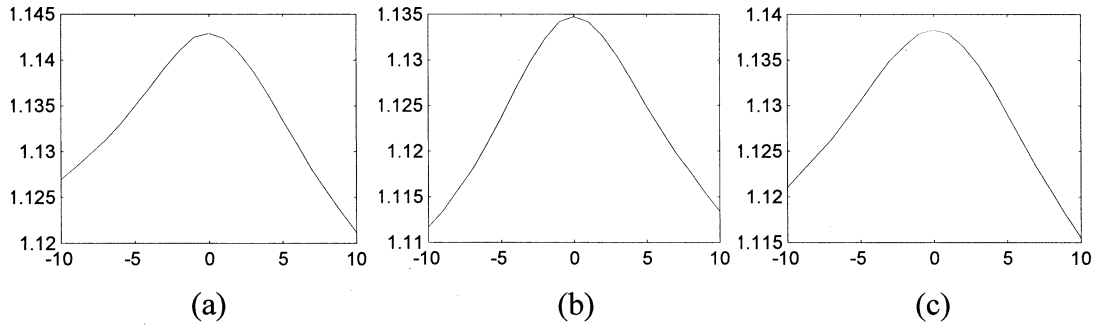

Fig. 7. Registration functions of CT_PD registration of patient_004-patient_006 using second-order GPVE algorithm. Notice that no artifact pattern can be observed in either (b) or(c). In each case, x axis is the displacement in millimeters and y axis is the MI measure.

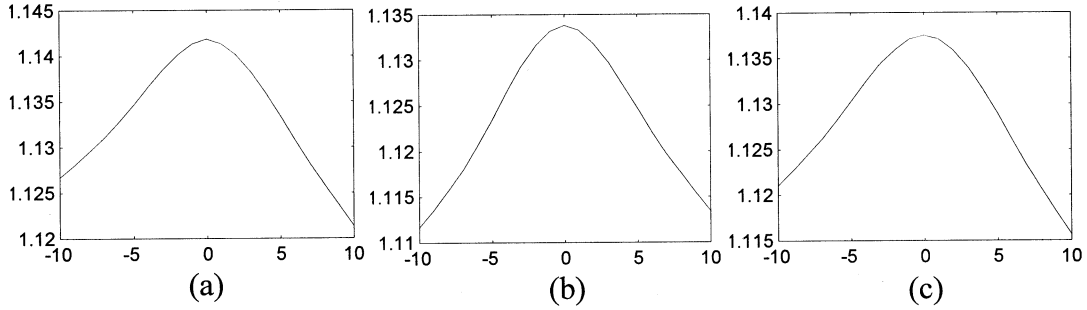

Fig. 8. Registration functions of CT-PD registration of patient_004-patient_006 using the third-order GPVE algorithm. Notice that no artifact pattern can be observed in either (b) or (c). In each case, x axis is the displacement in millimeters and y axis is the MI measure.

respectively. In this case, significant improvement over the PVI algorithm in registration accuracy is achieved.

In the case that the "visual influence on accuracy" column indicates "mild," the artifacts are present but the influence on the accuracy is not certain. This influence may be either negative or positive as explained in Section I. In this case, the mean registration errors are 1.5788, 1.5963, and 1.5964 mm. The explanation for this is that, in this case, the location of the true global maximum α_{ideal} is close to the location of the maximum α_{arti} determined in the presence of artifacts. In other words, it is a coincidence that the PVI results in such accuracy. This is consistent with the observation made in [16]. To support our claim, we can observe the *PS* measures for those "*mild*" cases (shown in italic) in which PVI outperforms either the second or third GPVE. The average *PS* measure in these cases is less then 0.1 mm, which means the true global maximum is likely to be very close to the maximum determined in the presence of the artifacts. This supports our explanation for the relatively small loss when higher order GPVE schemes are used in the "mild" case. In the third case, where the artifact pattern is absent, the mean registration errors are 2.2769, 2.1446, and and 2.2035 mm, respectively, which shows a limited improvement in the accuracy.

TABLE VII
REGISTRATION ERRORS FOR RECTIFIED IMAGE DATA

	First order (PV interpolation) error (mm)	Second order error (mm)	Third order error (mm)
CT_PD_rectified	0.86	0.87	0.83
CT_T1_rectified	0.82	0.75	0.74
CT_T2_rectified	1.04	0.97	1.01

To further compare the registration accuracy of the PVI algorithm (first-order GPVE) with the second and third GPVE algorithms in general (no artifacts), registration results from the rectified MR images of the same patients can be used. No artifacts

are anticipated using the rectified MR image volume because the MR volumes are rescaled during the rectification process [21]. Table VII lists the mean registration errors over the seven patients using different joint histogram estimation schemes. From this, we observe that the accuracies of higher order GPVEs are essentially the same as the PVI algorithm.

VII. Concluding Remarks

MI-based image registration has become an important tool for medical imaging applications. In many instances, interpolation induced artifacts appear that hamper the optimization process and influence registration accuracy. In this paper, we have presented a joint histogram estimation scheme that is specifically designed for use with the MI-based registration algorithm. This method employs higher order B-spline kernels during the estimation of the joint histogram. It should be stressed that the motive here is not to better approximate the point spread function (psf) but to reduce the abrupt change of the joint histogram dispersion caused by the PVI method. It is also the reason that it is sufficient to apply higher order kernel along the z direction only for the Vanderbilt University furnished brain image data, since it is the z direction in which abrupt change of the joint histogram dispersion occurs when PVI is used.

We have evaluated the effectiveness of our approach by applying it to the brain image data provided by Vanderbilt University for brain CT to MR image registration application. We employ the first-, second-, and third-order GPVE algorithms and compare their registration accuracies and their abilities to suppress interpolation-induced artifacts. Our experimental results indicate that in the presence of artifacts that clearly affect registration accuracy, the use of higher order GPVE algorithms suppresses the artifacts and improves registration accuracy considerably. In the absence of artifacts, the registration accuracy achieved by PVI and higher orders GPVE algorithms are essentially the same. Thus, we have proposed a joint histogram estimation method for MI-based image registration that exhibits excellent performance in the presence of artifacts as evident from our experimental findings.

Acknowledgment

The authors would like to thank the anonymous reviewers for their valuable comments and suggestions to improve the paper. The images and the standard transformation(s) were provided as part of the project, "Retrospective Image Registration Evaluation," National Institutes of Health, Project Number 8R01EB002124-03, Principal Investigator, J. Michael Fitzpatrick, Vanderbilt University, Nashville, TN.

References

[1] G. Q. Maguire, Jr., M. E. Noz, H. Rusinek, J. Jaeger, E. L. Kramer, J. J. Sanger, and G. Smith, "Graphics applied to medical image registration," *IEEE Comput. Graph. Applicat.*, vol. 11, pp. 20–28, Mar. 1991.

[2] L. G. Brown, "A survey of image registration techniques," *ACM Computing Surveys*, vol. 24, no. 4, pp. 325–376, 1992.

[3] H. Chen and P. K. Varshney, "Automatic two stage IR and MMW image registration algorithm for concealed weapon detection," *Inst. Elect. Eng. Proc., Vision, Image and Signal Processing*, vol. 148, no. 4, pp. 209–216, Aug. 2001.

[4] F. Maes, A. Collignon, D. Vandermeulen, G. Marchal, and P. Suetens, "Multimodality image registration by maximization of mutual information," *IEEE Trans. Med. Imag.*, vol. 16, pp. 187–198, Apr. 1997.

[5] W. M. Wells, P. Viola, H. Atsumi, and S. Nakajima, "Multi-modal volume registration by maximization of mutual information," *Med. Image Anal.*, vol. 1, no. 1, pp. 35–51, 1996.

[6] C. Studholme, D. L. G. Hill, and D. J. Hawkes, "Automated three-dimensional registration of magnetic resonance and positron emission tomography brain images by multiresolution optimization of voxel similarity measures," *Med. Phys.*, vol. 24, no. 1, pp. 25–35, Jan. 1997.

[7] M. Holden, D. L. G. Hill, E. R. E. Denton, J. M. Jarosz, T. C. S. Cox, T. Rohlfing, J. Goodey, and D. J. Hawkes, "Voxel similarity measures for 3-D serial MR brain image registration," *IEEE Trans. Med. Imag.*, vol. 19, pp. 94–102, Feb. 2000.

[8] H. Chen and P. K. Varshney, "A pyramid approach for multimodality image registration based on mutual information," in *Proc. 3rd Int. Conf. Information Fusion*, vol. I, July 2000, pp. MoD3 9–MoD3 15.

[9] C. Studholme, D. L. G. Hill, and D. J. Hawkes, "An overlap invariant entropy measure of 3D medical image alignment," *Pattern Recogn.*, vol. 32, pp. 71–86, 1999.

[10] F. Maes, "Segmentation and registration of multimodal medical images: From theory, implementation and validation to a useful tool in clinical practice ," Ph.D. dissertation, Catholic Univ. Leuven, Leuven, Belgium, 1998.

[11] C. E. Rodríguez-Carranza and M. H. Loew, "A weighted and deterministic entropy measure for image registration using mutual information," in *Proc. SPIE Conf. Image Processing*, Feb. 1998, pp. 155–166.

[12] A. Roche, G. Malandain, and N. Ayache, "Unifying maximum likelihood approaches in medical image registration," *Int. J. Imag. Syst. Technol.*, vol. 11, no. 1, pp. 71–80, 2000.

[13] P. Thevenaz and M. Unser, "Optimization of mutual information for multiresolution image registration," *IEEE Trans. Image Processing*, vol. 9, pp. 2083–9, Dec. 2000.

[14] J. L. Boes and C. R. Meyer, "Multi-variate mutual information for registration," in *Lecture Notes in Computer Science"*. Berlin, Germany: Springer-Verlag, 1999, vol. 1679 , Medical Image Computing and Computer-Assisted Intervention—MICCAI'99, Second International Conference Proceedings, pp. 606–12.

[15] M. B. Skouson, Q. Guo, and Z. Liang, "A bound on mutual information for image registration," *IEEE Trans. Med. Imag.*, vol. 20, pp. 843–846, Aug. 2001.

[16] J. P. W. Pluim, J. B. A. Maintz, and M. A. Viergever, "Interpolation artefacts in mutual information-based image registration," *Comput. Vis. Image Understanding*, vol. 77, pp. 211–232, 2000.

[17] R. G. Keys, "Cubic convolution interpolation for digital image processing," *IEEE Trans. Acoust., Speech, Signal Processing*, vol. ASSP-29, pp. 1153–60, Dec. 1981.

[18] M. Unser, A. Aldroubi, and M. Eden, "B-spline signal processing: Part I-theory," *IEEE Trans. Signal Processing*, vol. 41, pp. 821–833, Feb. 1993.

[19] ——, "B-spline signal processing: Part II-efficient design," *IEEE Trans. Signal Processing*, vol. 41, pp. 834–848, Feb. 1993.

[20] H. Chen and P. K. Varshney, "Registration of multimodal brain images: Some experimental results," in *SPIE Conf. Sensor Fusion: Architectures, Algorithms and Applications VI*, vol. 4731, Apr. 2002, pp. 122–133.

[21] J. West *et al.*, "Comparison and evaluation of retrospective intermodality brain image registration techniques," *J. Comput. Assist. Tomogr.*, vol. 21, no. 4, pp. 554–566, 1997.

[22] Vanderbilt Univ., Nashville, TN. Retrospective Image Registration Evaluation (RIRE). [Online]. Available: http://www.vuse.vanderbilt.edu/~image/registration/

[23] T. M. Cover and J. A. Thomas, *Elements of Information Theory*: Wiley, 1991.

[24] McConnell Brain Imag. Centre Montreal Neurological Inst, McGill Univ., Montreal, QC, Canada.. [Online]. Available: http://www.bic.mni.mcgill.ca/brainweb/

[25] D. L. Collins, A. P. Zijdenbos, V. Kollokian, J. G. Sled, N. J. Kabani, C. J. Holms, and A. C. Evans, "Design and construction of a realistic digital brain phantom," *IEEE Trans. Med. Imag.*, vol. 17, pp. 463–468, June 1998.

[26] C. R. Maurer, Jr., J. M. Fitzpatrick, M. Y. Wang, R. L. Galloway, Jr., R. J. Maciunas, and G. S. Allen, "Registration of head volume images using implantable fiducial markers," *IEEE Trans. Med. Imag.*, vol. 16, pp. 447–62, Aug. 1997.

[27] J. A. Nelder and R. Mead, "A simplex method for function minimization," *Comput. J.* , vol. 7, no. 4, pp. 308–313, 1965.